

Spectral Analysis for Semantic Segmentation with Applications on Feature Truncation and Weak Annotation

Li-Wei Chen[†], Wei-Chen Chiu[†], Chin-Tien Wu^{†‡}

[†] Department of Computer Science, National Yang Ming Chiao Tung University, Hsin-Chu, Taiwan

[‡] Department of Applied Mathematics, National Yang Ming Chiao Tung University, Hsin-Chu, Taiwan

lwchen6309.cs07@nycu.edu.tw, walon@cs.nctu.edu.tw, ctw@math.nctu.edu.tw

Abstract

It is well known that semantic segmentation neural networks (SSNNs) produce dense segmentation maps to resolve the objects' boundaries while restrict the prediction on down-sampled grids to alleviate the computational cost. A striking balance between the accuracy and the training cost of the SSNNs such as U-Net exists. We propose a spectral analysis to investigate the correlations among the resolution of the down sampled grid, the loss function and the accuracy of the SSNNs. By analyzing the network back-propagation process in frequency domain, we discover that the traditional loss function, cross-entropy, and the key features of CNN are mainly affected by the low-frequency components of segmentation labels. Our discoveries can be applied to SSNNs in several ways including (i) determining an efficient low resolution grid for resolving the segmentation maps (ii) pruning the networks by truncating the high frequency decoder features for saving computation costs, and (iii) using block-wise weak annotation for saving the labeling time. Experimental results shown in this paper agree with our spectral analysis for the networks such as DeepLab V3+ and Deep Aggregation Net (DAN).

1 Introduction

Semantic segmentation, which densely assigns semantic labels to each image pixel, is one of the important topics in computer vision. Recently we have witnessed that the CNNs based on the encoder-decoder architecture (Long, Shelhamer, and Darrell 2015; Chen et al. 2018; Badrinarayanan, Kendall, and Cipolla 2017; Zhao et al. 2017; Chen et al. 2014; Yang et al. 2018; Noh, Hong, and Han 2015; Yu and Koltun 2015) achieve striking performance on several segmentation benchmarks (Mottaghi et al. 2014; Everingham et al. 2015; Cordts et al. 2016; Zhou et al. 2017; Caesar, Uijlings, and Ferrari 2018). The existing works, *e.g.* Fully Convolutional Neural Network (FCN) (Long, Shelhamer, and Darrell 2015), U-Net (Ronneberger, Fischer, and Brox 2015), and DeepLab models (Chen et al. 2014; Chen et al. 2017; Chen et al. 2018), utilize encoder-decoder architecture to resolve the dense map. Generally, an encoder-decoder architecture consists of an encoder module that gradually reduces the spatial resolution of features for extracting context information and a decoder module that aggregates the information from the encoder and recovers

the spatial resolution of the dense segmentation map. On the other hand, these networks predict the dense segmentation map on a **low-resolution grid (LRG)**, *e.g.* $\frac{1}{4}$ and $\frac{1}{8}$ of the original image resolution, which is then up-sampled to the original image resolution, to save the computational cost (Chen et al. 2018; Long, Shelhamer, and Darrell 2015). Besides the LRG for prediction, some of networks can learn sufficient semantic contents from the weak annotations such as the annotation with coarse contours of objects (Papandreou et al. 2015; Dai, He, and Sun 2015; Khoreva et al. 2017) or those annotations derived from the image level (Ahn and Kwak 2018; Jing, Chen, and Tian 2019; Zhou et al. 2019; Shimoda and Yanai 2019; Sun et al. 2019; Nivaggioli and Randrianarivo 2019) to save the labeling cost. These weak annotations based on the coarse contour actually equivalent to the annotation obtained by applying LRG onto the pixel-wise groundtruth annotation. Despite the labeling inaccuracy near object boundary induced by LRG, the existing works demonstrate that networks can still achieve comparable accuracy with those networks that learn from the pixel-wise groundtruth annotation. Hence, these results indicate significance of LRG for either prediction or annotation for saving the cost with negligible accuracy loss.

Despite the success on using LRG for prediction and annotation, *i.e.* weak annotations, for cost saving, it yet remains unclear how these approaches affect the accuracy of the trained networks in theory and why LRG is significant. In the sense of spectral (Fourier) analysis, LRG for prediction and annotation actually associates with the low-frequency component of segmentation maps. On the other hand, the labeling inaccuracy near object boundary associates with the high-frequency component of segmentation maps. We hence suspect that the significance of LRG actually corresponds to the learning tendency of networks for the low-frequency signals. In fact, the existing works of spectral analysis demonstrate that the network tends to learn the low-frequency component of target signal in the regression of the uniformly distributed data with various frequencies (Rahaman et al. 2018; Ronen et al. 2019; Luo et al. 2019; Yang and Salman 2019; Xu et al. 2019). Such tendency is known as spectral bias (Rahaman et al. 2018). However, the spectral bias remains unclear for semantic segmentation since the distribution of segmentation annotation is not necessarily uniformly distributed along frequencies regimes. To

verify our speculation on the spectral bias of segmentation networks, we perform a spectral analysis on a semantic segmentation networks.

In this work, we present a theoretical analysis on the influence of the LRG to the network prediction and identify important features through our theoretical results. More specifically, we investigate the correlations among the frequency distributions of ground truth annotation and network output segmentation, the objective function (*e.g.* cross-entropy (CE)), the evaluation metric (*e.g.* intersection-over-union (IoU) score), and the resolution of CNN features in the frequency domain. We summarize the following key observations:

- The cross-entropy (CE) can be explicitly decomposed into the summation of frequency components. We find that CE is mainly contributed by the low-frequency component of segmentation maps.
- Spectral analysis of IoU score reveals its close relation to the CE. This results justify that the segmentation networks are trained upon CE while evaluated upon IoU.
- The correlation between the segmentation logits and the features within CNNs, in the frequency domain, shows that the segmentation logits of a specific frequency are mainly affected by the features within the same frequency.
- Based on the findings above, the high frequency components of smooth features are found to be less important. Truncating these high frequency components does not interfere the performance of semantic segmentation networks.

Our findings above contribute to the semantic segmentation networks in the following two objectives:

1. **Feature truncation for segmentation networks.** The features in the decoder can be truncated since they are generally assumed to be smooth comparing to the ones in the encoder. This truncation method can be easily integrated with the commonly-used pruning approaches (Liu et al. 2019; He et al. 2019) for further cost reduction. Moreover, one can determine the efficient size of LRG by spectral analysis.
2. **Block-wise annotation.** For semantic segmentation, it is easier to collect a weak annotation that keeps the low-resolution information of the full pixel-wise ground truth annotation. The block-wise annotation can be directly associated with the low frequency spectral information. We propose a block-wise annotation that emulating the existing weak annotations, where only the coarse contours of the instances in the segmentation map (Papandreou et al. 2015; Khoreva et al. 2017) are used, and show that the segmentation networks trained via these block-wise annotations are still efficient and accurate.

We relegates the review of related work such as segmentation network, *i.e.* SSNN, network pruning and spectral bias in section A.1 of appendix. We present the proposed analysis in section 2 and the above applications in section 3. The experimental results are expected in our analysis.

2 Proposed Spectral Analysis

To clearly depict the efficacy of LRG, we analyze the formalism of cross-entropy (CE) objective function and the intersection-over-union (IoU) evaluation metric in frequency domain. We demonstrate the analysis of CE in section 2.1 while relegate the analysis of IoU in section A.3 of appendix. Our results show that CE can be decomposed into the components of frequencies and positively correlate to IoU score; this justifies the usage of CE as objective function and IoU as evaluation metric in the network training framework. Moreover, as CE is decomposed into the components of frequencies, we investigate the learning mechanism for various frequency component. We deduce the gradient propagation for convolutional layers in frequency domain and demonstrate the correlation between the segmentation output and the features in CNNs in section 2.2. Our results suggest that the high-frequency components of the features and annotations have less influence on the performance of the segmentation networks due to the band limit introduced by the LRG. Finally, we conclude the spectral analysis upon segmentation networks in section 2.3.

Notation. The notations in this section are defined as follows. In general, the upper case letter, *e.g.* X, Y, Z, B , denote the functional in the spatial domain t while the lower case letter *e.g.* x, y, z, b , denote the corresponding spectrum in the frequency domain ν . For example, the spectrum $y(\nu) = \mathcal{F}(Y(t))$ where \mathcal{F} is the Fourier transform operator. The rest of notations will be defined whenever they appear.

2.1 Spectral Decomposition of Cross-Entropy

Let $Y(t, c)$ denote the segmentation logits produced by a semantic segmentation network and $B(t, c)$ denote the groundtruth annotation, in which c and t are indexes for the object class and image pixel respectively. The commonly-used objective function for learning semantic segmentation, cross-entropy (CE), can be written as

$$\begin{aligned} \mathcal{L}_{CE} &= -\sum_c \int B(t, c) \log\left(\frac{e^{Y(t, c)}}{\sum_c e^{Y(t, c)}}\right) dt \\ &= -\sum_c \int B(t, c) (Y(t, c) - Y_p(t)) dt, \end{aligned} \quad (1)$$

where $Y_p(t) = \log(\sum_c e^{Y(t, c)})$. Transforming this integral into frequency domain ν gives theorem 1. See proof of theorem 1 in section A.2 of appendix.

Theorem 1 (Spectral decomposition of Cross-Entropy). *Given Y the segmentation logits and B the groundtruth annotation, the cross-entropy \mathcal{L}_{CE} can be decomposed as $\mathcal{L}_{CE} = \sum_\nu \mathcal{L}_{ce}(\nu)$, where $\mathcal{L}_{ce}(\nu)$ is the **frequency components of CE** and can be computed as following,*

$$\mathcal{L}_{ce}(\nu) = \sum_c b(-\nu, c) (y_p(\nu) - y(\nu, c)) \quad (2)$$

here, b , y , and y_p are the spectra of B , Y , and Y_p , respectively.

The contribution from each frequency components to CE can thus be evaluated. In addition, it follows immediately that $\mathcal{L}_{ce}(\nu)$ is small when either $y_p(\nu) - y(\nu, c)$ or $b(\nu, c)$ is small. For simplicity, let $\widehat{y}(\nu, c) = y_p(\nu) - y(\nu, c)$. Recalls that, as mentioned in section 1, $Y(t, c)$ is generally predicted upon the low-resolution grid. Hence, $\widehat{y}(\nu_i, c)$, as well as $\mathcal{L}_{ce}(\nu_i)$, should be small at high-frequency ν_i . Besides, the magnitude of high frequency components of the ground truth annotation is generally small dues to the intrinsic smoothness of segmentation map¹. One can therefore conclude that \mathcal{L}_{CE} is the mainly contributed by the low-frequency components. This conclusion will be validated later in section 3.1 and lead us to the first key observation. Furthermore, it follows from this observation that the significance of high-frequency component of pixel-wise groundtruth to \mathcal{L}_{CE} is negligible. This also explain why weak annotation, which drop the high-frequency component of segmentation map, can be an effective approach to pixel-wise groundtruth annotation. Most of researches in studying weak annotations (Papandreou et al. 2015; Dai, He, and Sun 2015; Khoreva et al. 2017; Guo et al. 2021; Lu et al. 2021; Ahn and Kwak 2018; Jing, Chen, and Tian 2019; Zhou et al. 2019; Shimoda and Yanai 2019; Sun et al. 2019; Nivaggioli and Randrianarivo 2019) demonstrate efficacy of WA solely by experiments on benchmark datasets. Here, our spectral analysis further provide a theoretical foundation to the WA.

Besides the analysis of CE, we further perform the analysis of IoU score and correlate it to the analysis of CE in section A.3. The analysis reveals how the minimization of CE correlates to the maximization of IoU score. This observation justifies the rationality of the common learning procedure for semantic segmentation networks: the networks are trained by the CE objective function while being validated by the IoU scores. This corresponds to the second key observation. Therefore, later in our experiments and analysis, we adopt the decomposition of CE to study the frequency response and take IoU as a reasonable metric for evaluation.

2.2 Spectral Gradient of Convolutional Layers

In section 2.1, we have demonstrated that the CE can be decomposed into the summation of frequency components $\mathcal{L}_{ce}(\nu)$. Here we further deduce the gradient propagation of $\mathcal{L}_{ce}(\nu)$ within CNNs in order to reveal how $\mathcal{L}_{ce}(\nu)$ updates the network, especially for the gradient in low-frequency regime. We hereafter refer the gradient propagation with respect to input feature X in frequency domain as the **spectral gradient**. With this, we can analyze how the low-frequency of input feature affect the network performance. For simplicity, we deduce the spectral gradient for a convolutional layer, including a convolution and an activation function

$$\begin{aligned} Z(t) &= K(t) \otimes X(t) \\ Y(t) &= \sigma(Z(t)), \end{aligned} \tag{3}$$

¹Segmentation map usually consists of several segment for each class. All the internal region of segment is flat while only the regions near the segmentation boundaries contain high-frequency components.

where K is the kernel, σ is the activation function, X is input feature, and Y is the output of convolutional layer. We consider the soft-plus activation $\sigma(Z(t)) = \log(1 + e^{Z(t)})$ since its everywhere differentiable thus make it easier for analysis. The spectral gradient for a convolutional layer is given as below.

Theorem 2 (The spectral gradient for a convolutional layer). *Given B the groundtruth annotation, X , K and Y as in Eq. 3, the spectral gradient of $\mathcal{L}_{ce}(\nu)$ the frequency components of CE is*

$$\frac{\partial \mathcal{L}_{ce}(\nu_i)}{\partial x(\nu_j)} \simeq \sum_c \frac{1}{2} k(\nu_j, c) [D_0(\nu_i) s(-\nu_j, c) - \delta_{\nu_j}(\nu_i) b(-\nu_i, c)], \tag{4}$$

and the spectral gradient of y the output is

$$\frac{\partial y(\nu_i)}{\partial x(\nu_j)} \simeq \frac{1}{2} k(\nu_j) \delta_{\nu_j}(\nu_i), \tag{5}$$

assuming the $K(t)$ is small and $|X(t)| < 1$,² where $y(\nu) = \mathcal{F}(Y(t))$, $b(\nu) = \mathcal{F}(B(t))$, $k(\nu) = \mathcal{F}(K(t))$, $x(\nu) = \mathcal{F}(X(t))$, and $s(\nu) = \mathcal{F}(S(t))$ the spectrum of segmentation output. $\delta_{\nu_j}(\nu_i)$ is the Kronecker delta function, which is here after abbreviated as the delta function, and $D_0(\nu_i)$ is the Dirac delta function.

We relegate the proof of Eq. 5 in lemma 5 of appendix and that of Eq. 4 in lemma 6 of appendix. Clearly from the theory, the spectral gradient in Eq. 5 can be approximated as the delta function, indicating $y(\nu_i)$ is affected only by $x(\nu_i)$ with the same frequency. This corresponds to the third key observation. Now, let us further analyze how the variation of feature $x(\nu_j)$ affect $\mathcal{L}_{ce}(\nu_i)$ based on Eq. 4. For simplicity, we consider the case $\nu_i \neq 0$ and $\nu_i = 0$ separately. This reveals the contribution of the feature to network performance and provides a guideline for removing the redundant feature. For $\nu_i \neq 0$, the gradient becomes

$$\frac{\partial \mathcal{L}_{ce}(\nu_i)}{\partial x(\nu_j)} \simeq - \sum_c \frac{1}{2} k(\nu_j, c) \delta_{\nu_j}(\nu_i) b(-\nu_i, c), \text{ if } \nu_j \neq 0, \tag{6}$$

which indicates that the CNN feature $x(\nu_j)$ is affected only by $\mathcal{L}_{ce}(\nu_i)$ with same frequency. For $\nu_i = 0$, the gradient consists of additional term $\sum_c \frac{1}{2} k(\nu_j, c) D_0(\nu_i) s(-\nu_j, c)$. Here recalls that the segmentation map $s(\nu, c)$ is usually predicted upon the low-resolution grid of the original image as mentioned in section 1. $s(\nu, c)$ should therefore be smooth so that $s(-\nu_j, c)$ is small when ν_j is large. Hence,

$$\frac{\partial \mathcal{L}_{ce}(\nu_i)}{\partial x(\nu_j)} \ll 1, \text{ if } \nu_j \text{ is large and } \nu_j \neq \nu_i = 0. \tag{7}$$

It follows from Eq. 6 and Eq. 7 that the CNN feature $x(\nu_j)$ is affected only by $\mathcal{L}_{ce}(\nu_i)$ with near frequency. Thus, removing the features $x(\nu_j)$ at high-frequency ν_j does not effect $\mathcal{L}_{ce}(\nu_i)$ at low-frequency ν_i . This give us the forth

²These assumptions rely on the fact that the numeric scale of feature and kernel are usually limited to a small range of value for the numeric stability of networks.

key observation. With this observation, it becomes possible to reduce the feature size of CNN, as well as its high-frequency components, while keep the performance. We further provide the numerical validation of this observation in section 3.1.

2.3 Discussion for Spectral Analysis

In this section, we summarize the discussion for the spectral analysis based on the theoretical analysis in the above sections. Recalls the segmentation map is usually predicted upon the LRG of the original image. Here we aim to determine the efficient LRG that efficiently reduce the the cost reduction while preserve accuracy. Following the decomposition of CE in Eq. 13, we define the truncated CE as the frequency components of CE filtered by LRG

$$\hat{\mathcal{L}}_{CE}(\nu_{max}) = \sum_{\nu}^{\nu_{max}} \mathcal{L}_{ce}(\nu), \quad (8)$$

where ν_{max} is the band limit that corresponds to $2\nu_{max}$ LRG size. Further, we define

$$R(\nu_{max}) = |1 - \frac{\hat{\mathcal{L}}_{CE}(\nu_{max})}{\mathcal{L}_{CE}}| \quad (9)$$

as the losses of \mathcal{L}_{CE} due to the truncation at band limit ν_{max} . Hence, an efficient LRG can be defined when $R(\nu_{max})$ is negligible. One can apply LRG to either segmentation outputs or groundtruth annotation to alleviate cost. In addition, these LRG can further be applied to the features in CNNs to save computational cost follows from the forth key observation discussed in section 2.2. In the following section, we apply the efficient LRG on the features and the groundtruth annotation and validate the positive correlation between the the loss of CE and the loss of IoU score caused by LRG.

3 Validation and Applications

This section aims to validate the spectral analysis in section 2 and further propose the application, including the feature truncation and block-wise annotation. In section 3.1, we validate the spectral analysis in section 2, including the frequency components of CE in Eq. 2 and the spectral gradient in Eq. 4. The validation of $\mathcal{L}_{ce}(\nu)$ the frequency components of CE demonstrates that CE is mainly contributed by the low-frequency component while the validation of $\frac{\partial \mathcal{L}_{ce}(\nu_i)}{\partial x(\nu_j)}$ the spectral gradient shows that it can be well approximated as the delta function as in Eq. 7. Based on these numeric validations, we identify the efficient LRGs and apply the grids onto the features in CNNs and the groundtruth annotation. This leads us to further propose two applications that downsample the segmentation maps into LRGs: (1) Feature truncation and (2) Block-wise annotation, which detailed in section 3.2 and section 3.3, respectively.

Datasets and Segmentation Networks. We examine the experiments upon the following three semantic segmentation datasets: PASCAL semantic segmentation benchmark (Everingham et al. 2015), DeepGlobe land-cover classification

challenge (Demir et al. 2018) and Cityscapes pixel-level semantic labeling task (Cordts et al. 2016) (denoted as PASCAL, DeepGlobe and Cityscapes respectively). For segmentation networks, we utilize DeepLab v3+ (Chen et al. 2018) and Deep Aggregation Net (DAN) (Kuo et al. 2018). See section A.8 of appendix for implementation details.

3.1 Validation of Spectral Analysis

Spectral Decomposition of CE. This section aims to demonstrate that CE is mainly contributed by the low-frequency component, as discussed in section 2.1, and investigate the efficacy of using the LRG for prediction by the modern networks. We evaluate $|b(\nu)|$, $|\hat{y}(\nu)|$, $\mathcal{L}_{ce}(\nu)$ and $R(\nu_{max})$ based on the various segmentation networks (DeepLab v3+ and DAN) and datasets (PASCAL, DeepGlobe and Cityscapes); $|b(\nu)|$ and $|\hat{y}(\nu)|$ are the averaged power spectrum of $b(\nu, c)$ and $\hat{y}(\nu, c)$ over all semantic classes c respectively. The results are shown in Fig. 1.³ To monitor the training progress, the evaluation at both the initial and final stages of network training are additionally shown in Fig. 2. The results shown in Fig. 1 indicate that

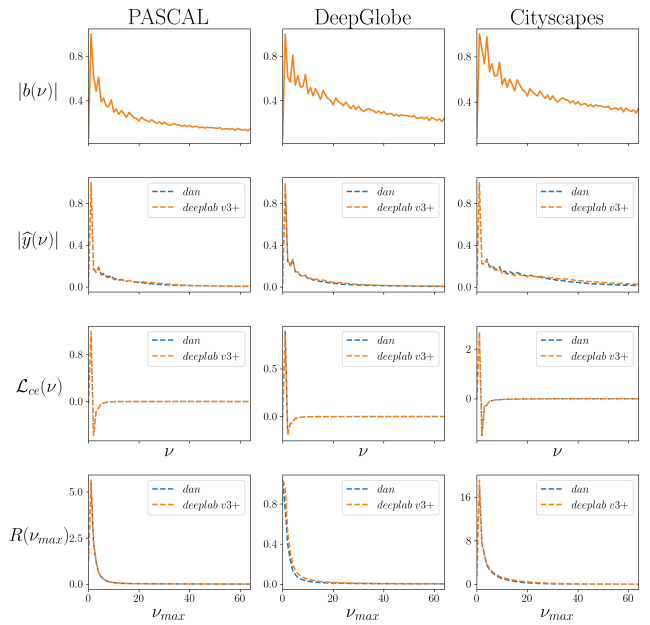


Figure 1: The spectral decomposition of CE ($\mathcal{L}_{ce}(\nu)$), the relative discrepancy of CE ($R(\nu_{max})$), and the absolute value of spectra ($|b(\nu)|$ and $|\hat{y}(\nu)|$). The profiles of $|\hat{y}(\nu)|$, $\mathcal{L}_{ce}(\nu)$, and $R(\nu_{max})$ are evaluated based on DeepLab v3+ and DAN.

$|\hat{y}(\nu)|$ is indeed small in the high-frequency region thus leads to small $\mathcal{L}_{ce}(\nu)$, as discussed above. These results also support the fact that CE is mainly contributed by the low-frequency components. On the other hands, the results

³The profiles of $|b(\nu)|$ and $|\hat{y}(\nu)|$ are normalized with respect to their corresponding maximal values for better comparison over datasets.

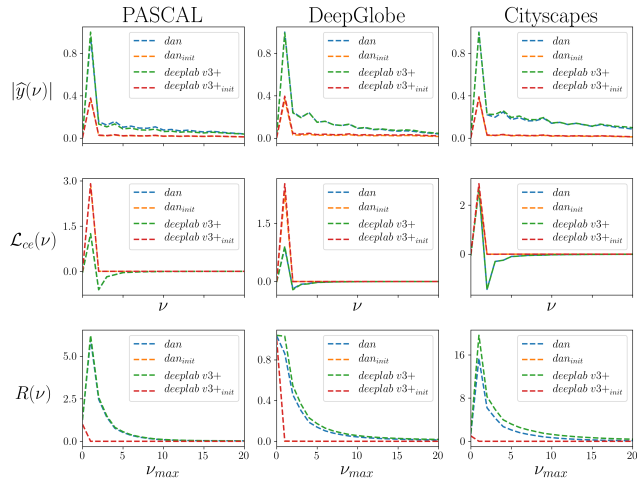


Figure 2: Spectral Decomposition of CE for DeepLab v3+ and DAN at both initial and final training stages. The notation follows Fig. 1. The suffix $_{init}$ additionally denotes the profiles of the network at initial stage.

shown in Fig. 2 reveals that the low-frequency components of $\mathcal{L}_{ce}(\nu)$ apparently decreases as training progresses, suggesting the spectral bias for semantic segmentation, *i.e.* networks learn to capture low-resolution-grid more effectively.

Table 1: Truncated CE and its relative discrepancy with respect to CE under various band limit ν , based on the PASCAL, DeepGlobe and Cityscapes datasets.

Dataset	ν_{max}	8	16	32	64	256
DeepLab v3+						
PASCAL	$R(\nu_{max})$	0.184	0.040	0.017	0.008	0
DeepGlobe	$R(\nu_{max})$	0.053	0.017	0.007	0.003	0
Cityscapes	$R(\nu_{max})$	1.782	0.517	0.065	0.014	0
DAN						
PASCAL	$R(\nu_{max})$	0.197	0.045	0.017	0.008	0
DeepGlobe	$R(\nu_{max})$	0.078	0.025	0.009	0.004	0
Cityscapes	$R(\nu_{max})$	2.004	0.723	0.153	0.017	0

Here we further investigate the efficacy of LRGs for prediction based on $R(\nu_{max})$ examined in Fig. 1. For comparison, we examine the numeric value of $R(\nu_{max})$ in Table 1. Note that $\mathcal{L}_{ce} = \hat{\mathcal{L}}_{ce}(256)$ due to the image size 513 in our experiments.

Apparently, as the resolution of the grid goes higher, $R(\nu_{max})$ becomes smaller since more information on high-frequency is captured. More specifically, $R(\nu_{max})$ dramatically decrease to small values when $\nu > 10$ in all experiments of the trained networks. On the other hand, the segmentation maps predicted by these networks are evaluated on the 129×129 LRG that corresponds to $\nu_{max} = 64$. These empirical evidences suggest that the LRGs with $10 < \nu_{max} < 64$ could still efficiently sample the segmentation map without significant information loss. These efficient LRGs are further validated on our proposed applications, *i.e.* feature truncation and block-wise annotation, in sections 3.2 and section 3.3, respectively. Besides, it is apparent from Table 1 that $R(\nu_{max})$ on the Cityscapes dataset

is significantly larger than that on the PASCAL and DeepGlobe datasets. We shall expect a better efficacy of the feature truncation and the block-wise annotation on the PASCAL and DeepGlobe datasets.

Spectral Gradient. We now turn to evaluate the gradient introduced in section 2.2, including $\frac{\partial y(\nu_i)}{\partial x(\nu_j)}$ in Eq. 5 and $\frac{\partial \mathcal{L}_{ce}(\nu_i)}{\partial x(\nu_j)}$ in Eq. 4. We demonstrate that both $\frac{\partial y(\nu_i)}{\partial x(\nu_j)}$ and $\frac{\partial \mathcal{L}_{ce}(\nu_i)}{\partial x(\nu_j)}$ can be approximated as the delta function. We validate these spectral gradients on the three datasets (PASCAL, DeepGlobe and Cityscapes datasets) and take the spectra of ASPP (atrous spatial pyramid pooling) features in DeepLab v3+ and DAN as our example $x(\nu_j)$. The evaluated $\frac{\partial \mathcal{L}_{ce}(\nu_i)}{\partial x(\nu_j)}$ for DeepLab v3+ and DAN are illustrated in Fig. 3a and Fig. 3b, respectively. Besides, we validate $\frac{\partial y(\nu_i)}{\partial x(\nu_j)}$ for various operations within the decoder module of these networks, including the convolution, ReLU, bilinear up-sampling, where $x(\nu_j)$ and $y(\nu_i)$ denote the input and output spectra for these operations, respectively. These spectral gradients are illustrated in Fig. 4. For all the spectral gradients shown in Fig. 3a, Fig. 3b and Fig. 4, the frequency $\nu_i = (0, \frac{M}{4}, \frac{M}{2})$ are evaluated as examples, where M is the size of input features. We set $M = 33$ in this experiment. For each ν_i , we evaluate the spectral gradient for all frequencies ν_j in region from 0 to $\frac{M}{2}$. This results in a matrix of spectral gradient for each ν_i , which is shown in each row respectively.

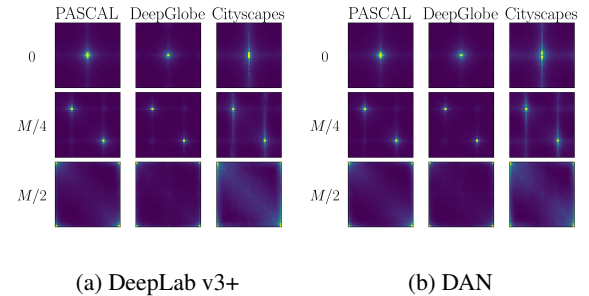


Figure 3: The evaluation of spectral gradient $\frac{\partial \mathcal{L}_{ce}(\nu_i)}{\partial x(\nu_j)}$ for DeepLab v3+ and DAN. The spectral gradient are evaluated based on PASCAL, DeepGlobe and Cityscapes datasets.

We can see from Fig. 4 that $\frac{\partial y(\nu_i)}{\partial x(\nu_j)}$ for the convolution, ReLU and bilinear up-sampling are delta function for all ν_i , which is consistent with our discussion for Eq. 5. Moreover, clearly from Fig. 3a and Fig. 3b, the spectral gradient $\frac{\partial \mathcal{L}_{ce}(\nu_i)}{\partial x(\nu_j)}$ that accumulating all the operations in the decoder module can be well approximated by the delta function. These results verify the approximation of Eq. 4 and agrees the discussion in section 2.2 that the feature component at frequency ν_i only affects $\mathcal{L}_{ce}(\nu)$ at the frequency near ν_i , which enable us to further consider the removal of redundant high-frequency feature in section 3.2.

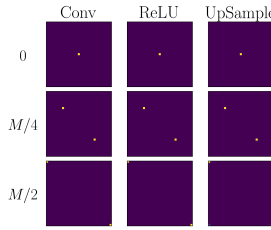


Figure 4: The evaluation of spectral gradient $\partial y(\nu_i)/\partial x(\nu_j)$. The spectral gradient for the convolution, ReLU, and bilinear up-sampling operations are denoted as Conv, ReLU, Up-sample, respectively.

3.2 Application on Feature Truncation

We propose the feature truncation as a model reduction method that reduce the cost of model without degrading the performance. The feature truncation is intuitively performed by removing the high-frequency components of the decoder features $x(\nu)$ acquired from the in the $R(\nu_{max})$ evaluated in section 3.1. We further adopt the Soft Filter Punning (SFP) method (He et al. 2019) and combine it with feature truncation as an example. The experiments are done based on the following conditions: For SFP, we use pruning rate [20%, 40% and 60%] for the encoder while use 20% for the decoder since parameters of the encoder is much larger than that of the decoder and is potentially over-parameterized. For the feature truncation applied on the decoder, we down-sample the decoder features from the original size of 129×129 to the efficient LRGs suggested by the analysis in section 3.1, *i.e.* the LRGs with $10 < \nu_{max} < 64$. All the down-sampling are done via bilinear interpolation. For simplicity, the experiments mentioned above are only tested on the LRG 65×65 and 33×33 that correspond to the band limit $\nu_{max} = 32$ and $\nu_{max} = 16$, respectively. The feature size of decoder are [33, 65, 129] in the setup of feature truncation. The FLOPs of these experiments are summarized in Table 2a, where "Baseline" model denotes the model without SFP. Clearly, the feature truncation effective reduce the FLOPs at various setups of SFP. We further evaluate the relative FLOPs-drop, which is the relative reduction rate of FLOPs comparing to that of the model with same SFP setup and the original feature size 129, in Table 2b. For example, the relative FLOPs-drop of the setup with "60% Pruning rate for encoder" and feature size "33" based upon DeepLab v3+ is given as $1 - \frac{29}{59} = 50.5\%$. As the feature truncated from 129 to 65, the relative FLOPs-drop are 23.3% and 7.9% for the "Baseline" model of DeepLab v3+ and DAN, respectively. As the pruning rate of encoder goes to 60%, the relative FLOPs-drop even increases to 50.5% and 24.9% for the two models, respectively. Noting that the number parameters of decoder are 1.3 and 0.4 million for the two models, respectively. Apparently, the cost reduction rates by feature truncation depend on the number parameters in the decoder. The more parameters in the decoder, the better efficacy of feature truncation is achieved. These results demonstrate an effective cost reduction combining the

pruning method (SFP) and feature truncation.

DeepLab v3+			
SFP setups \ Feature size	129	65	33
Baseline	139	107	98
20% Pruning rate for encoder	100	76	70
40% Pruning rate for encoder	77	53	47
60% Pruning rate for encoder	59	35	29

DAN			
SFP setups \ Feature size	129	65	33
Baseline	107	98	96
20% Pruning rate for encoder	78	70	69
40% Pruning rate for encoder	55	47	46
60% Pruning rate for encoder	37	29	28

(a) FLOPs for the models with SFP and feature truncation; denoted in unit of 10^9 FLOPs

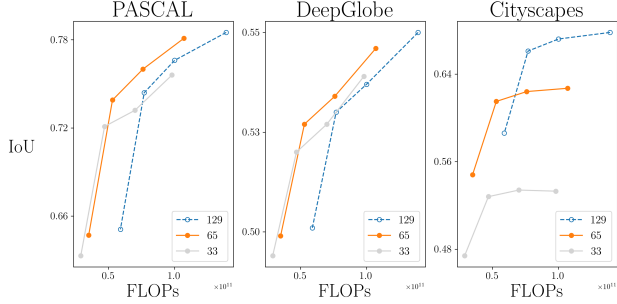
DeepLab v3+			
SFP setups \ Feature size	129	65	33
Baseline	0.0%	23.3%	29.2%
20% Pruning rate for encoder	0.0%	23.7%	29.8%
40% Pruning rate for encoder	0.0%	30.9%	38.7%
60% Pruning rate for encoder	0.0%	40.3%	50.5%

DAN			
SFP setups \ Feature size	129	65	33
Baseline	0.0%	7.9%	9.8%
20% Pruning rate for encoder	0.0%	9.4%	11.7%
40% Pruning rate for encoder	0.0%	13.4%	16.7%
60% Pruning rate for encoder	0.0%	19.9%	24.9%

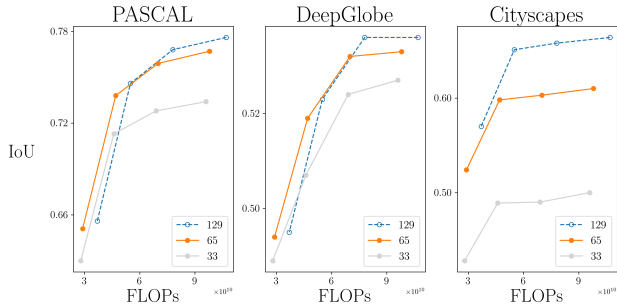
(b) Relative FLOPs-drop caused by feature truncation.

Table 2: FLOPs reduction.

On the other hand, such huge cost reduction indispensably degrade the model performance. We evaluate DeepLab v3+ and DAN upon the PASCAL, DeepGlobe and Cityscapes datasets. Figure 5 illustrates the IoU score of these models with respect to the FLOPs; we provide the numeric details in Table 4a and Table 4b of appendix. For the DeepLab model, the feature truncation with feature size 65 efficiently decrease the FLOPs while keep the IoU score compared to the original model upon the PASCAL and DeepGlobe datasets. In contrast, the truncation partly fails to preserve the IoU score on the Cityscapes dataset, which actually consists to the analysis of $R(\nu_{max})$ in Table 1, *i.e.* the relative loss of CE effected by LRG; where the $R(\nu_{max})$ for the DeepLab model on the Cityscapes dataset is significantly larger than the other datasets. We discuss the correlation between the IoU drop and the analysis of $R(\nu_{max})$ in section A.9 of appendix. Besides, the truncation with feature size 33 reduce the FLOPs while also leads to apparent IoU drop thus make the overall efficacy unclear. For the feature truncation for the DAN model, the overall efficacy is also unclear since the reduction of FLOPs are relatively smaller than those of DeepLab while the leading IoU drop is non-negligible. To further estimate the efficiency of feature truncation for these models that simultaneously includes the cost and performance, we define **FLOPs per IoU score (FPI)** as FLOPs/mIoU. The lower the FPI, the better the efficiency of the model that minimizes the performance drop while maximizes the cost reduction of inference. The FPI of these models are illustrated in Fig. 6a and Fig. 6b. For the experiments on PASCAL and DeepGlobe datasets, the FPI decreases as



(a) DeepLab v3+

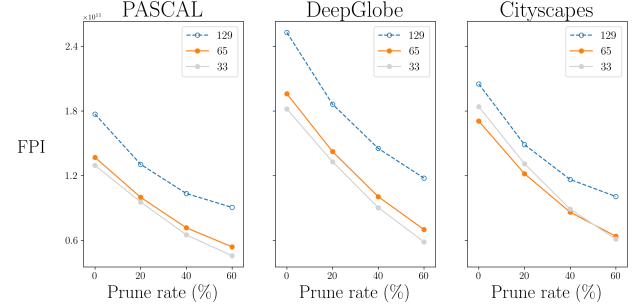


(b) DAN

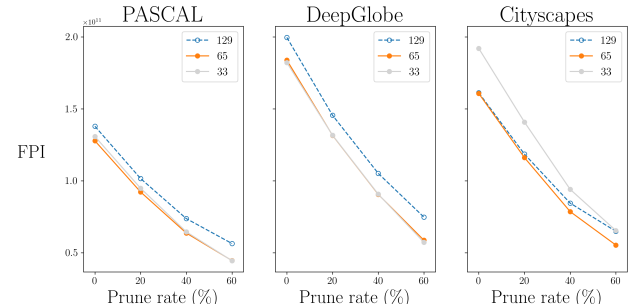
Figure 5: IoU vs. FLOPs for DeepLab v3+ and DAN with various prune rates of SFP and feature size (*i.e.* 33, 65, 129) for the feature truncation.

feature truncated from 129 to either 65 or 33. In comparison, the decrements of FPI on the Cityscapes dataset is apparently smaller than those on the other datasets. Moreover, the FPI instead increases as feature truncated from 129 to 33 for the experiment of DAN on the Cityscapes dataset. These results consist with our analysis on $R(\nu_{max})$ discussed in section 3.1. On the other hand, the results indicates that the feature truncation effectively reduce the computational cost on PASCAL and DeepGlobe datasets with significant reduction of FPI.

In summary, we conclude that the integration of feature truncation and SFP can efficiently reduce the computational cost when $R(\nu_{max})$ is small as demonstrated on the PASCAL and DeepGlobe datasets. On the other hand, it becomes inefficient when $R(\nu_{max})$ is relatively large as demonstrated on the Cityscapes dataset. Our theoretical analysis on $R(\nu_{max})$ can help to estimate the efficacy of feature truncation for neural networks such as DeepLab v3+ and DAN. To our understanding, this is the first work that provide a theoretical framework to analyze the segmentation performance in the aspect of the frequency domain. As mentioned in section 1, the existing segmentation networks predict the segmentation maps upon the LRG to save the computational cost. Our framework serves as a analysis tool to estimate the efficient LRG size of segmentation maps as well as the effective features in decoders in saving the computational cost. Furthermore, such analysis can be further generalized to arbitrary features in CNNs.



(a) DeepLab v3+



(b) DAN

Figure 6: The FPI for DeepLab v3+ and DAN with the same setups as in Figure 5.

3.3 Application on Block-wise annotation

In section 3.1, we determine the efficient LRG for the segmentation maps via analyzing $R(\nu_{max})$. In this section, we apply these LRGs to the groundtruth annotations. The resulted block-wise annotation can be considered as a weak annotation. We demonstrate that the performance of the semantic segmentation network trained with these block-wise annotations can also be estimated by $R(\nu_{max})$. We perform the experiment that trains DeepLab v3+ and DAN with the block-wise annotation at various band limit ν_{max} (from 8 to 256) and evaluates the $R(\nu_{max})$ based on the original pixel-wise annotation. Examples of the block-wise annotation and the prediction of the two models upon the PASCAL, DeepGlobe and Cityscapes datasets are illustrated in Fig. 7. Note that the block-wise annotation at $\nu_{max} = 256$ is actually equivalent to the original pixel-wise groundtruth. The experimental results are summarized in Table 3. For each ν_{max} , we evaluate mIoU score and mIoU drop. Particularly, mIoU-drop is the reduction rate of mIoU with respect to the one band limit $\nu_{max} = 256$; this drop actually corresponds to the decrements of IoU score caused by the LRG on the annotation. As the band limit ν_{max} goes lower, mIoU score goes smaller and a positive mIoU drop is observed. Here we also observe a significant larger amount of mIoU drop on the Cityscapes dataset comparing to those on the PASCAL and DeepGlobe datasets, which consists to the trend of $R(\nu_{max})$ in Table 1 that $R(\nu_{max})$ on the Cityscapes dataset are significantly larger than the other datasets. Fig. 8 illustrates the correlation between rela-

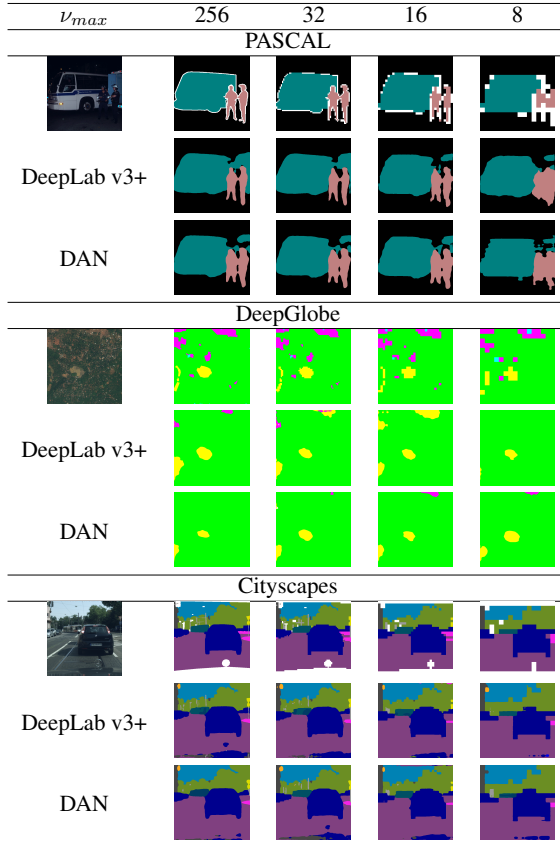


Figure 7: Examples of the block-wise annotation and the prediction of DeepLab v3+ and DAN. For each dataset, we present the block-wise groundtruth annotations and the predictions of these models. The corresponding band limits ν_{max} are denoted at the top of annotation.

tive mIoU drops and $R(\nu_{max})$ for all experiments. The positive correlation between mIoU drop and $R(\nu_{max})$ agrees the correlation between CE and IoU score discussed in section A.3. Our studies show that the performance of the semantic segmentation network trained with the block-wise annotation strongly correlates to $R(\nu_{max})$. As a result, one can estimate the performance of the semantic segmentation network trained with the block-wise annotation by simply evaluating $R(\nu_{max})$ without thoroughly performing the experiments over all band limits.

In summary, the proposed spectral analysis enables the advanced analysis of weak annotation in the frequency domain. Our studies reveal the correlation between the segmentation performance and the LRG of segmentation maps. Based on our analysis and experiments, the block-wise annotation can be considered as a weak annotation when the block size is chosen according to the LRG size in the segmentation maps. Notably, these LRGs actually correspond to the coarse contour of instances in the segmentation maps, which are greatly utilized in the existing weak annotation. We provide the theoretical justification of the weak annotations by using our spectral analysis. Further research

ν_{max}	8	16	32	256
DeepLab v3+				
PASCAL	67.4%	74.2%	77.1%	78.5%
DeepGlobe	52.5%	53.8%	54.8%	55.0%
Cityscapes	38.4%	50.5%	58.9%	67.8%
DAN				
PASCAL	67.6%	74.0%	76.5%	77.6%
DeepGlobe	50.1%	52.2%	53.4%	53.6%
Cityscapes	38.4%	50.4%	58.3%	66.4%

ν_{max}	8	16	32	256
DeepLab v3+				
PASCAL	14.1%	5.4%	1.8%	0.0%
DeepGlobe	4.6%	2.3%	0.3%	0.0%
Cityscapes	43.4%	25.4%	13.1%	0.0%
DAN				
PASCAL	12.9%	4.6%	1.4%	0.0%
DeepGlobe	6.5%	2.6%	0.3%	0.0%
Cityscapes	42.1%	24.2%	12.2%	0.0%

(a) mIoU score.

ν_{max}	8	16	32	256
DeepLab v3+				
PASCAL	14.1%	5.4%	1.8%	0.0%
DeepGlobe	4.6%	2.3%	0.3%	0.0%
Cityscapes	43.4%	25.4%	13.1%	0.0%
DAN				
PASCAL	12.9%	4.6%	1.4%	0.0%
DeepGlobe	6.5%	2.6%	0.3%	0.0%
Cityscapes	42.1%	24.2%	12.2%	0.0%

(b) relative mIoU-drop.

Table 3: Experimental results of using our proposed block-wise annotation for learning semantic segmentation.

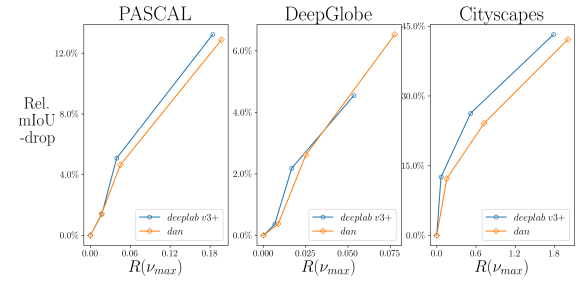


Figure 8: The correlation between relative IoU-drop and the $R(\nu_{max})$ for block-wise annotation.

should be undertaken to investigate the spectral analysis upon the existing weak annotations (Papandreou et al. 2015; Khoreva et al. 2017) in the future.

4 Conclusion

Our proposed spectral analysis for semantic segmentation network correlate CE, IoU score and gradient back-propagation in the spectrum point of view. We first explicitly decompose CE and demonstrate the CE is mainly contributed by the low-frequency component of the segmentation maps, which associates with the features in CNNs at the same frequency. Furthermore, we proposed $R(\nu_{max})$ to estimate the efficacy of the LRG for segmentation maps. We test our theory on two applications: feature truncation and block annotation. Our results show that combination of the feature truncation and the network pruning can save computational cost significantly with small accuracy lost. In addition, the block annotation can potentially save more in labeling cost, since the network trained using the block-wise annotation in an efficient LRG performs close to the original network. The results from our experiments agree with our theoretical predictions based on $R(\nu_{max})$. Lastly, despite the theoretical analysis and validation in this work, it remains unclear

that how to determine the efficient band limit ν_{max} of the LRG for various datasets. It would be our future interests to estimate ν_{max} from the spectrum of groundtruth annotation.

A Appendix

A.1 Related Work

Semantic Segmentation Neural Network Among semantic segmentation neural networks (SSNN), Long et al. first propose Fully Convolutional Neural Network (FCN) (Long, Shelhamer, and Darrell 2015) that predicts the dense segmentation map by utilizing the skip-architecture, where the features of different granularities in the encoder are up-sampled and integrated in the decoder, yet still faces the challenge of acquiring accurate object boundaries in the segmentation map. The similar idea can be also observed in the U-Net (Ronneberger, Fischer, and Brox 2015), which further adds dense skip-connections between the corresponding down-sampling and up-sampling modules of the same feature dimensions, in results the boundary localization is improved but not fully resolved yet. Other than skip connections, Chen et al. propose the DeepLab models (Chen et al. 2014; Chen et al. 2017; Chen et al. 2018) that integrate the atrous spatial pyramid pooling module (ASPP), which utilizes the dilated convolutional layer composed of the filters at multiple sampling rates thus having the contextual information at the various spatial resolution, to boost the edge-response at object boundaries. Kou et al. further propose Deep Aggregation Net (DAN) that utilize an aggregation decoder and progressively combines encoder features for final prediction to resolve the land cover segmentation across image scales. Besides of these SSNNs, extra modules such as dense conditional random field (dense CRF) (Chen et al. 2014; Krähenbühl and Koltun 2011) and PointRend (Kirillov et al. 2019) can be further applied to boost the edge-response near object boundaries while induce extra computational cost. It is clear that improving edge-response near object boundaries becomes a main challenge of semantic segmentation while the cost of SSNNs grows dues to the dense decoder feature and post processing modules. This work investigate the spectral analysis and computation cost of DeepLab v3+ and DAN. We briefly review the cost of these SSNNs in the next section.

Network Pruning Network pruning (Liu et al. 2019; He et al. 2019; Molchanov et al. 2019; Blalock et al. 2020; Zhao et al. 2019; Luo, Wu, and Lin 2017; Karnin 1990; Han et al. 2015) is proposed to reduce the cost of inference by removing the redundant network parameters. The redundant parameters are determined when either their contribution to output (Molchanov et al. 2019; Luo, Wu, and Lin 2017; Zhao et al. 2019) or their norm (He et al. 2019) are negligible. Noting that most of these pruning method are by hard pruning, *i.e.* remove some weight values of filters (Han et al. 2015) or completely remove the whole filters (Luo, Wu, and Lin 2017), while potentially degrading the capacity of networks. In contrast, He et al. (He et al. 2019) propose the soft pruning method that dynamically set redundant parameters to zero while keep the network capacity. This enables the compressed network to have a larger optimization space

and make it easier for the model to learn from the training data, and achieve higher accuracy.

Despite the success of these methods for accelerating network, we would like to point out that the existing pruning methods are solely investigated upon image classification (Krizhevsky, Hinton, and others 2009; Russakovsky et al. 2015) instead of other task, such as semantic segmentation or image generation. We further investigate the application of pruning methods on semantic segmentation in this work. Noting the the segmentation networks typically have huge parameters in encoder while negligible parameters in decoder (Chen et al. 2018; Kuo et al. 2018; Long, Shelhamer, and Darrell 2015). However, the computational costs of decoders are often comparable to those of encoders since it up-samples the features for the dense segmentation map and results in large features for computation. For example, the encoder of DeepLab v3+ (Chen et al. 2018) has 95.6 billion FLOPs (floating-point operations) and 60.1 million parameters. In contrast, its decoder has 43.4 billion FLOPs while only has 1.3 million parameters. Similarly, the encoder of DAN (Kuo et al. 2018) has 95.6 billion FLOPs with 60.1 million parameters while the decoder has 11.1 billion FLOPs with only 0.4 million parameters. The proposed feature truncation in section 3.2 is thus expected to effectively reduce the computational cost. Moreover, one can combine feature truncation with the typical network pruning method to reduce the computation cost in two different aspects, *i.e.* the feature size and the redundant parameters.

Spectral Analysis The existing works of spectral analysis demonstrate that the network tends to learn the low-frequency component of target signal in the regression of the uniformly distributed data with various frequencies (Rahaman et al. 2018; Ronen et al. 2019; Luo et al. 2019; Yang and Salman 2019; Xu et al. 2019). Such tendency is known as spectral bias (Rahaman et al. 2018) or Frequency Principle(Xu et al. 2019). More specifically, these works found that the network tend to learn low-frequency signal in the earlier training stage. Ronen et al. (Ronen et al. 2019) further provide the theoretical explanation based normalized training data that is uniformly distributed on a hypersphere. Under same assumption of data distribution, Yang and Salman (Yang and Salman 2019) further investigate the eigen function of neural tangent kernel (NTK) (Jacot, Gabriel, and Hongler 2018) and demonstrate that the eigenvalue of NTK decrease as the frequency increases. This provide further theoretical insight and justify the spectral bias that the learning of networks converge faster for low-frequency signals.

So far, the existing works investigate the spectral bias solely under the normalized training data with uniform distribution over frequency regime. This work further extends spectral analysis to semantic segmentation, where the target data is non-uniformly distributed. Furthermore, these works mostly study the convergence speed for each frequency regime while this work focus on the learned distribution of networks at final training stage. This helps us to estimate the capacity of models, in the sense of frequency, under the spectral bias in semantic segmentation.

A.2 Proof of Theorem 1

Theorem 1 (Spectral decomposition of Cross-Entropy). *Given Y the segmentation logits and B the groundtruth annotation, the cross-entropy \mathcal{L}_{CE} can be decomposed as $\mathcal{L}_{CE} = \sum_{\nu} \mathcal{L}_{ce}(\nu)$, where $\mathcal{L}_{ce}(\nu)$ is the **frequency components of CE** and can be computed as following,*

$$\mathcal{L}_{ce}(\nu) = \sum_c b(-\nu, c)(y_p(\nu) - y(\nu, c)) \quad (2)$$

here, b , y , and y_p are the spectra of B , Y , and Y_p , respectively.

Proof. Given Y and B , \mathcal{L}_{CE} the cross-entropy is

$$\begin{aligned} \mathcal{L}_{CE} &= -\sum_c \int B(t, c) \log\left(\frac{e^{Y(t, c)}}{\sum_c e^{Y(t, c)}}\right) dt \\ &= -\sum_c \int B(t, c)(Y(t, c) - Y_p(t)) dt, \end{aligned} \quad (10)$$

where $Y_p(t) = \log(\sum_c e^{Y(t, c)})$. For all $Y(t) \in Y(t, c)$ and $B(t) \in B(t, c)$, the integral $\int Y(t)B(t)dt$ can be transformed to the frequency domain ν as follows. (See lemma 3 of appendix)

$$\int Y(t)B(t) dt = \int y(z) b(-z) dz \quad (11)$$

where $y(\nu)$ and $b(\nu)$ are the spectrum of the segmentation logits and that of the groundtruth annotations, respectively. The \mathcal{L}_{CE} in Eq. 1 is hence given by

$$\begin{aligned} \mathcal{L}_{CE} &= -\sum_c \int B(t, c)(Y(t, c) - Y_p(t)) dt \\ &= \sum_c \int b(-\nu, c)(y_p(\nu) - y(\nu, c)) d\nu. \end{aligned} \quad (12)$$

The discrete integral of Eq. 12 gives us the decomposition of the \mathcal{L}_{CE} over frequency domain ν as following

$$\begin{aligned} \mathcal{L}_{CE} &= \sum_{\nu} \sum_c b(-\nu, c)(y_p(\nu) - y(\nu, c)) \\ &= \sum_{\nu} \mathcal{L}_{ce}(\nu), \end{aligned} \quad (13)$$

where

$$\mathcal{L}_{ce}(\nu) = \sum_c b(-\nu, c)(y_p(\nu) - y(\nu, c)). \quad (14)$$

□

A.3 Spectral Analysis of Intersection-over-Union Score

Given the segmentation logits Y and the groundtruth annotation B , the intersection-over-union (IoU) score is typically defined as $\frac{|B \cap S|}{|B \cup S|}$, where S is the segmentation output $S(t, c) = \frac{e^{Y(t, c)}}{\sum_c e^{Y(t, c)}}$. It is common to train the network with CE and evaluate the network performance based on IoU scores. This section aims to analyze the formalism of IoU

score in frequency domain and shed some light to the reason why IoU scores can be increased when the CE is decreased.

In order to analyze the IoU score in the frequency domain, we extend the above definition to the continuous space as follows:

$$\begin{aligned} IoU(S, B) &= \frac{\int B(t)S(t) dt}{\int B(t) + S(t) dt - \int B(t)S(t) dt} \\ &= \frac{1}{\frac{\int B(t) + S(t) dt}{\int B(t)S(t) dt} - 1} \end{aligned} \quad (15)$$

where t denotes pixel indexes. Eq. 15 holds for each object class c . Here we skip c for simplicity. Notably, this definition is equivalent to the origin definition of IoU score for the binarized segmentation maps. The components in Eq. 15 can be written as follows (see lemma 3 and lemma 4 of appendix),

$$\begin{aligned} \int B(t)S(t) dt &= \int s(\nu)b(-\nu) d\nu, \text{ and} \\ \int B(t) + S(t) dt &= b(0) + s(0), \end{aligned} \quad (16)$$

where $s(\nu) = \mathcal{F}(S(t))$. As a result, IoU score can be written as

$$IoU(s, b) = \frac{1}{\frac{s(0) + b(0)}{\int s(\nu)b(-\nu) d\nu} - 1} \quad (17)$$

and it is composed of two terms: $s(0) + b(0)$ and $\int s(\nu)b(-\nu) d\nu = \int B(t)S(t) dt$. It can be seen that the IoU score can not be explicitly decomposed as the case for CE in Eq. 13 due to the non-linearity of Eq 17. On the other hand, noting that the latter term, *i.e.* $\int s(\nu)b(-\nu) d\nu = \int B(t)S(t) dt$, positively correlates to $\int B(t) \log(S(t)) dt$ the component of CE in Eq. 1 since the \log function is monotonically increasing. Hence, minimal \mathcal{L}_{CE} maximizes $\int B(t)S(t) dt$ as well as IoU score. Besides the analysis of IoU score, we also analyze the boundary IoU (Cheng et al. 2021) in the next section. The analysis demonstrate that the boundary IoU is mainly contributed by the low-frequency component of segmentation maps, similar to the analysis of CE. This demonstrate the boundary IoU is not only sensitive to object boundary, as highlighted in (Cheng et al. 2021), while being also sensitive to smooth region, *i.e.* low-frequency component, of segmentation maps.

A.4 Spectral Analysis of Boundary Intersection-over-Union Score

Following the notation in section A.3, the boundary intersection-over-union (Boundary IoU) (Cheng et al. 2021) score is defined as

$$\text{boundary IoU} = \frac{|(B \cap B_d) \cap (S \cap S_d)|}{|(B \cap B_d) \cup (S \cap S_d)|}, \quad (18)$$

where S_d and B_d denote the pixels in the boundary region of S and B , respectively; d is the width of boundary region. Compared to IoU score, such evaluation metric is shown to be sensitive to the boundary especially for the large object.

In addition to its sensitivity to object boundary, this section reveals its theoretical insight and demonstrate that it's mainly contributed by the low-frequency component of segmentation map.

Without loss of generality, we analyze the 1 dimensional case of boundary IoU. We consider the binary segmentation map as follows,

$$\begin{aligned} S &= H(t - t_{s0}) - H(t - t_{s1}), t_{s0} < t_{s1} \\ B &= H(t - t_{b0}) - H(t - t_{b1}), t_{b0} < t_{b1} \end{aligned} \quad (19)$$

where H is the Heaviside function; t_{s0} and t_{s1} are the boundary pixels of S ; t_{b0} and t_{b1} are the boundary pixels of B ; we model the boundary region of segmentation map by two gaussian function for each boundary edge. Namely,

$$\begin{aligned} \Omega_S &= S_d \cap S = e^{-\frac{(t-t_{s0})^2}{2\sigma^2}} + e^{-\frac{(t-t_{s1})^2}{2\sigma^2}} \\ \Omega_B &= B_d \cap B = e^{-\frac{(t-t_{b0})^2}{2\sigma^2}} + e^{-\frac{(t-t_{b1})^2}{2\sigma^2}} \end{aligned} \quad (20)$$

where $\sigma = \sigma(d)$ is the width of gaussian associating with the d in S_d and B_d mentioned above. We have their Fourier transform as

$$\begin{aligned} \omega_s &= (e^{-j t_{s0} \nu} + e^{-j t_{s1} \nu}) e^{-\frac{\nu^2 \sigma^2}{2}} \\ \omega_b &= (e^{-j t_{b0} \nu} + e^{-j t_{b1} \nu}) e^{-\frac{\nu^2 \sigma^2}{2}} \end{aligned} \quad (21)$$

Following similar deduction as in Eq. 15 and Eq. 17, we have

$$\text{boundary IoU}(s, b) = \frac{1}{\frac{\omega_s(0) + \omega_b(0)}{\int \omega_s(\nu) \omega_b(-\nu) d\nu} - 1}, \quad (22)$$

where

$$\begin{aligned} \int \omega_s(\nu) \omega_b(-\nu) d\nu &= \frac{\sqrt{\pi}}{2\sigma} \left(\right. \\ &\quad e^{-\frac{(-t_{s0}+t_{b0})^2}{4\sigma^2}} \text{erf}(\nu\sigma - j\frac{(t_{b0}-t_{s0})}{2\sigma}) \\ &\quad + e^{-\frac{(-t_{s0}+t_{b1})^2}{4\sigma^2}} \text{erf}(\nu\sigma - j\frac{(t_{b1}-t_{s0})}{2\sigma}) \\ &\quad + e^{-\frac{(-t_{s1}+t_{b0})^2}{4\sigma^2}} \text{erf}(\nu\sigma - j\frac{(t_{b0}-t_{s1})}{2\sigma}) \\ &\quad \left. + e^{-\frac{(-t_{s1}+t_{b1})^2}{4\sigma^2}} \text{erf}(\nu\sigma - j\frac{(t_{b1}-t_{s1})}{2\sigma}) \right) \end{aligned} \quad (23)$$

by plugging the Eq. 21; erf is the error function. Similar to Eq. 17, Eq. 22 consists of the zero-frequency part, i.e. $\omega_s(0) + \omega_b(0)$, and the non-zero frequency part, i.e. Eq. 23. We focus on analyzing the non-zero frequency part to further reveal the sensitivity of boundary IoU with respect to these frequency regime. Eq. 23 can be further approximated as

$$\begin{aligned} \int \omega_s(\nu) \omega_b(-\nu) d\nu &= \frac{\sqrt{\pi}}{2\sigma} \text{erf}(\nu\sigma) (e^{-\frac{(-t_{s0}+t_{b0})^2}{4\sigma^2}} \\ &\quad + e^{-\frac{(-t_{s0}+t_{b1})^2}{4\sigma^2}} + e^{-\frac{(-t_{s1}+t_{b0})^2}{4\sigma^2}} + e^{-\frac{(-t_{s1}+t_{b1})^2}{4\sigma^2}}) \end{aligned} \quad (24)$$

by using the expansion of erf function

$$\begin{aligned} \text{erf}(\nu\sigma - jC) &\simeq \text{erf}(\nu\sigma) + \\ &\quad \frac{e^{-\nu^2 \sigma^2}}{2\pi\nu\sigma} (1 - \cos(2\nu\sigma C) + j \sin(2\nu\sigma C)) \\ &\simeq \text{erf}(\nu\sigma) \end{aligned} \quad (25)$$

It follows immediately from Eq. 24 that $\int \omega_s(\nu) \omega_b(-\nu) d\nu$ is mainly contributed by low-frequency regime dues to erf function. This implies that boundary IoU is also mainly contributed by low-frequency regime while being sensitive to the object boundary.

A.5 Fourier transform of spatial integral

Lemma 3. Given two functional $Y(t)$ and $B(t)$ in spatial domain t , the overlapping integral $\int Y(t)B(t) dt$ can be transformed into the frequency domain ν as

$$\int Y(t)B(t) dt = \int y(z) b(-z) dz \quad (26)$$

where $y(\nu) = \mathcal{F}(Y(t))$ and $b = \mathcal{F}(B)$.

Proof. By the convolution lemma, integral $\int Y(t)B(t) dt$ can be written as

$$\int Y(t)B(t) dt = \int \mathcal{F}^{-1}(y(\nu) \otimes b(\nu)) dt \quad (27)$$

; where \otimes denotes the convolution operation as $y(\nu) \otimes b(\nu) = \int y(z) b(\nu - z) dz$; $\mathcal{F}^{-1}(y(\nu)) = \int y(\nu) e^{2j\pi\nu t} d\nu$ is the inverse Fourier transform operator; $j = \sqrt{-1}$. Eq. 27 can now be written as

$$\begin{aligned} \int Y(t)B(t) dt &= \int \int y(\nu) \otimes b(\nu) e^{2j\pi\nu t} d\nu dt \\ &= \int \int \int e^{2j\pi\nu t} y(z) b(\nu - z) dt d\nu dz \end{aligned} \quad (28)$$

By the orthogonality of Fourier basis, we have $\int e^{2j\pi\nu t} dt = D_0(\nu)$, where $D_0(\nu)$ is the Dirac delta function:

$$D_0(\nu) = \begin{cases} \infty, & \text{if } \nu = 0 \\ 0, & \text{otherwise} \end{cases} \quad (29)$$

and its integral property is $\int y(\nu) D_0(\nu) d\nu = y(0)$. Hence, Eq. 28 is given as

$$\begin{aligned} \int Y(t)B(t) dt &= \int \int y(z) b(\nu - z) D_0(\nu) d\nu dz \\ &= \int y(z) b(-z) dz \end{aligned} \quad (30)$$

□

Lemma 4. Given functional Y in spatial domain t , the integral $\int Y(t) dt$ can be transformed into the frequency domain ν as

$$\int Y(t) dt = y(0); \quad (31)$$

where $y(\nu) = \mathcal{F}(Y(t))$.

Proof. The proof follows similar process as for lemma 3, as follows.

$$\begin{aligned} \int Y(t) dt &= \int \mathcal{F}^{-1}(y(\nu)) dt \\ &= \int \int y(\nu) e^{2j\pi\nu t} d\nu dt \\ &= \int y(\nu) D_0(\nu) d\nu \\ &= y(0) \end{aligned} \quad (32)$$

□

A.6 Gradient propagation for a convolution layer

Consider a convolution layer consists of the convolutional kernel $K(t)$ and the soft-plus activation function $\sigma(z(t)) = \log(1 + e^{z(t)})$; t is the spatial location. Let X denote the input, the output of convolution layer is written as

$$\begin{aligned} Z(t) &= K(t) \otimes X(t) \\ Y(t) &= \sigma(Z(t)) \end{aligned} \quad (33)$$

Lemma 5. Assuming $K(t)$ is small and $|X(t)| < 1$, the spectral gradient can be approximated as

$$\frac{\partial y(\nu_i)}{\partial x(\nu_j)} \simeq \frac{1}{2} k(\nu_j) \delta_{\nu_j}(\nu_i), \quad (34)$$

where $z(\nu)$, $k(\nu)$, $x(\nu)$ and $\delta_{\nu_j}(\nu_i)$ are $\mathcal{F}(Z(t))$, $\mathcal{F}(K(t))$, $\mathcal{F}(X(t))$ and the Kronecker delta function, respectively.

Proof. The spectral gradient of a convolution layer consists of the spectral gradient for the convolution operator and that for the activation function. We will show two gradient and combine it in the end of derivation.

For the convolution operator, it can be written as in the frequency domain $z(\nu) = k(\nu)x(\nu)$, where $z(\nu)$, $k(\nu)$, and $x(\nu)$ are $\mathcal{F}(Z(t))$, $\mathcal{F}(K(t))$, and $\mathcal{F}(X(t))$, respectively. Without loss of generality, in the discrete frequency domain, the gradient of z under a specific frequency ν_i with respect to the x under frequency ν_j is defined as

$$\frac{\partial z(\nu_i)}{\partial x(\nu_j)} = \frac{\partial}{\partial x(\nu_j)}(k(\nu_i)x(\nu_i)) = k(\nu_i)\delta_{\nu_j}(\nu_i), \quad (35)$$

where $\delta_{\nu_j}(\nu_i)$ is the Kronecker delta function.

$$\delta_{\nu_j}(\nu_i) = \begin{cases} 1, & \text{if } \nu_i = \nu_j \\ 0, & \text{otherwise} \end{cases} \quad (36)$$

For the soft-plus function, it can be first expressed as Taylor series

$$\begin{aligned} \sigma(Z(t)) &= \log(1 + e^{Z(t)}) \\ &= \log(2) + \frac{1}{2}Z(t) + \frac{1}{8}Z(t)^2 + O(Z(t)^4), \end{aligned} \quad (37)$$

in which $Z(t)$ is small since the kernel $K(t)$ is small and $|X(t)| < 1$ by the assumption. Hence, $O(Z(t)^4)$ becomes negligible. The Fourier transform of $\sigma(Z(t))$ is thus given as

$$\begin{aligned} y(\nu) &= \mathcal{F}(\sigma(Z(t))) \\ &\simeq \mathcal{F}(\log(2) + \frac{1}{2}Z(t) + \frac{1}{8}Z(t)^2) \\ &= 2\pi\log(2)\delta_0(\nu) + \frac{1}{2}z(\nu) + \frac{1}{8}z(\nu) \otimes z(\nu), \end{aligned} \quad (38)$$

and its spectral gradient is

$$\begin{aligned} \frac{\partial y(\nu_i)}{\partial z(\nu_j)} &\simeq \frac{\partial}{\partial z(\nu_j)}(2\pi\log(2)\delta_0(\nu_i)) \\ &\quad + \frac{1}{2}z(\nu_i) + \frac{1}{8}z(\nu_i) \otimes z(\nu_i)) \\ &= \frac{\partial}{\partial z(\nu_j)}\left(\frac{1}{2}z(\nu_i) + \frac{1}{8}\sum_{r=0}^{n-1}z(\nu_i - \nu_r)z(\nu_r)\right) \\ &= \frac{1}{2}\delta_{\nu_j}(\nu_i) + \frac{1}{4}z(\nu_i - \nu_j), \end{aligned} \quad (39)$$

where r is a dummy variable for the convolution and n is the spectrum size of features. By Eq. 35 and Eq. 39, the spectral gradient of a convolutional layer in Eq. 3 is then written as

$$\begin{aligned} \frac{\partial y(\nu_i)}{\partial x(\nu_j)} &= \sum_{q=0}^n \frac{\partial y(\nu_i)}{\partial z(\nu_q)} \frac{\partial z(\nu_q)}{\partial x(\nu_j)} \\ &\simeq \sum_{q=0}^n \left(\left(\frac{1}{2}\delta_{\nu_q}(\nu_i) + \frac{1}{4}z(\nu_i - \nu_q) \right) k(\nu_q) \delta_{\nu_j}(\nu_q) \right) \\ &= k(\nu_j) \left[\frac{1}{2}\delta_{\nu_j}(\nu_i) + \frac{1}{4}z(\nu_i - \nu_j) \right], \end{aligned} \quad (40)$$

where i , j , and q are the frequency indices. Since $Z(t)$ is small as argued above, the corresponding spectrum $z(\nu)$ should also be small. We can therefore neglect the second term of Eq. 40, i.e. $\frac{1}{4}z(\nu_i - \nu_j)$, and approximate Eq. 40 as

$$\frac{\partial y(\nu_i)}{\partial x(\nu_j)} \simeq \frac{1}{2}k(\nu_j)\delta_{\nu_j}(\nu_i) \quad (41)$$

□

A.7 Gradient propagation for the frequency component of CE

Lemma 6. Given a convolutional layer that satisfies the assumption of lemma 5. Let $x(\nu)$ denote the spectrum of input feature. For each semantic class c in segmentation maps, let $k(\nu, c)$ and $y(\nu, c)$ denote the spectrum of kernel and that of the segmentation output, respectively. The spectral gradient for the frequency component of CE, $\mathcal{L}_{ce}(\nu_i)$ is

$$\frac{\partial \mathcal{L}_{ce}(\nu_i)}{\partial x(\nu_j)} \simeq \sum_c \frac{1}{2}k(\nu_j, c)[D_0(\nu_i)s(-\nu_j, c) - \delta_{\nu_j}(\nu_i)b(-\nu_i, c)], \quad (42)$$

where $\delta_{\nu_j}(\nu_i)$ is the Kronecker delta function and $D_0(\nu_i)$ is the Dirac delta function.

Proof. By lemma 5 and Eq. 2, the spectral gradient $\frac{\partial \mathcal{L}_{ce}(\nu_i)}{\partial x(\nu_j)}$ is given as

$$\begin{aligned} \frac{\partial \mathcal{L}_{ce}(\nu_i)}{\partial x(\nu_j)} &= \sum_c \sum_q \frac{\partial \mathcal{L}_{ce}(\nu_i)}{\partial y(\nu_q, c)} \frac{\partial y(\nu_q, c)}{\partial x(\nu_j)} \\ &\simeq \sum_c \sum_q \frac{1}{2} \frac{\partial \mathcal{L}_{ce}(\nu_i)}{\partial y(\nu_q, c)} k(\nu_j, c) \delta_{\nu_j}(\nu_q) \\ &= \sum_c \frac{1}{2} \frac{\partial \mathcal{L}_{ce}(\nu_i)}{\partial y(\nu_j, c)} k(\nu_j, c) \\ &= \sum_c \frac{1}{2}k(\nu_j, c) \frac{\partial \sum_{\tilde{c}} b(-\nu_i, \tilde{c})(y_p(\nu_i) - y(\nu_i, \tilde{c}))}{\partial y(\nu_j, c)} \\ &= \sum_c \frac{1}{2}k(\nu_j, c) \left[\left(\frac{\partial y_p(\nu_i)}{\partial y(\nu_j, c)} \sum_{\tilde{c}} b(-\nu_i, \tilde{c}) \right) \right. \\ &\quad \left. - \left(\sum_{\tilde{c}} \frac{\partial y(\nu_i, \tilde{c})}{\partial y(\nu_j, c)} b(-\nu_i, \tilde{c}) \right) \right], \end{aligned} \quad (43)$$

in which

$$\begin{aligned}
\frac{\partial y_p(\nu_i)}{\partial y(\nu_j, c)} &= \int \frac{\partial y_p(\nu_i)}{\partial Y(t, c)} \frac{\partial Y(t, c)}{\partial y(\nu_j, c)} dt \\
&= \int \frac{\partial \mathcal{F}(Y_p(t))}{\partial Y(t, c)} \frac{\partial \mathcal{F}^{-1}(y(\nu, c))}{\partial y(\nu_j, c)} dt \\
&= \int \frac{\partial \int \log(\sum_c e^{Y(t, c)}) e^{-2j\pi\nu_i t} dt}{\partial Y(t, c)} \\
&\frac{\partial \int y(\nu, c) e^{2j\pi\nu t} d\nu}{\partial y(\nu_j, c)} dt \\
&= \int \frac{e^{Y(t, c)}}{\sum_c e^{Y(t, c)}} e^{-2j\pi(\nu_i - \nu_j)t} dt \\
&= \int S(t, c) e^{-2j\pi(\nu_i - \nu_j)t} dt = s(\nu_i - \nu_j, c),
\end{aligned} \tag{44}$$

where $S(t, c)$ is the segmentation output after performing softmax on logits Y and $s(\nu, c)$ is the spectrum of the segmentation output. Further, we have

$$\sum_{\tilde{c}} b(-\nu_i, \tilde{c}) = D_0(\nu_i) \tag{45}$$

by the Fourier transform of $\sum_{\tilde{c}} B(t, \tilde{c}) = 1$, *i.e.* the fact that B denote the probability distribution over semantic classes and should sum to one for each pixel. Substituting Eq. 44 and Eq. 45 into Eq. 43, we have the overall spectral gradient as

$$\begin{aligned}
\frac{\partial \mathcal{L}_{ce}(\nu_i)}{\partial x(\nu_j)} &\simeq \sum_c \frac{1}{2} k(\nu_j, c) \\
&[D_0(\nu_i) s(-\nu_j, c) - \delta_{\nu_j}(\nu_i) b(-\nu_i, c)]
\end{aligned} \tag{46}$$

□

A.8 Implementation details

Datasets. We examine the experiments upon the following three semantic segmentation datasets: PASCAL semantic segmentation benchmark (Everingham et al. 2015), DeepGlobe land-cover classification challenge (Demir et al. 2018) and Cityscapes pixel-level semantic labeling task (Cordts et al. 2016) (denoted as PASCAL, DeepGlobe and Cityscapes respectively). The PASCAL dataset contains 21 categories, 1464 training images, and 1449 validation images; the dataset further augmented by the extra annotations from (Hariharan et al. 2011). The DeepGlobe dataset contains 7 categories, 803 training images, which are split into 701 and 102 images for training and validation, respectively. The Cityscapes dataset contains 19 categories, 2975 training images, and 500 validation images.

segmentation networks and implementation details. In our experiment, we utilize the standard segmentation networks including DeepLab v3+ (Chen et al. 2018) and Deep Aggregation Net (DAN) (Kuo et al. 2018). We adopt the ResNet-101 (He et al. 2016) pre-trained on ImageNet-1k (Russakovsky et al. 2015) as the backbone of these networks. These networks are trained by the following training policies: For all datasets, the images are randomly cropped

to 513×513 pixels; the training batch size are 8. For the PASCAL dataset, the network is trained with initial learning rate 0.0007 and 100 epochs; for DeepGlobe dataset, the network is trained with initial learning rate 0.007 and 600 epochs; for Cityscapes dataset, the network is trained with initial learning rate 0.001 and 200 epochs. For evaluation, the images are cropped to 513×513 pixels for all datasets for consistent image size in spectral analysis.

A.9 Discussion and Experimental Data of Feature Truncation

Table 4 summarize the experimental detail of feature truncation. For the experiment upon each dataset, the "mIoU" and "relative mIoU-drop" are evaluated, where "mIoU" is the mean IoU score over all semantic classes; "relative mIoU-drop" is the relative deduction rate of mIoU with respect to that of the model with same SFP setup and feature size 129. Apparently from the tables, the mIoU decreases as either the pruning rate increases or as the feature size decreases. Closer inspection of these tables show that the relative mIoU-drop of the experiments on the Cityscapes dataset are significantly larger than that on the PASCAL and DeepGlobe datasets. Taking the "Baseline" model of DeepLab v3+ with feature size 65 as an example, the relative mIoU-drop is 0.6% for both PASCAL and DeepGlobe datasets, while becomes 7.4% for the Cityscapes datasets. The same trends holds for the experiments with other SFP setup and feature size based on DeepLab v3+. Also, the similar results are observed in the experiment on DAN as shown in Table 4b. These significant mIoU-drop on Cityscapes is well explained by the theoretical estimation $R(\nu_{max})$ in Table 1, where $R(\nu_{max})$ depict the relative loss of CE evaluated that positively correlates to relative mIoU-drop as discussed in section A.3. We further illustrate the correlation between the relative mIoU-drop (cf. Table 4) and $R(\nu_{max})$ (cf. Table 1) in Fig. 9; where we plot the data with $\nu_{max} = [16, 32, 256]$. The positive correlation in the figure agrees our theoretical statement.

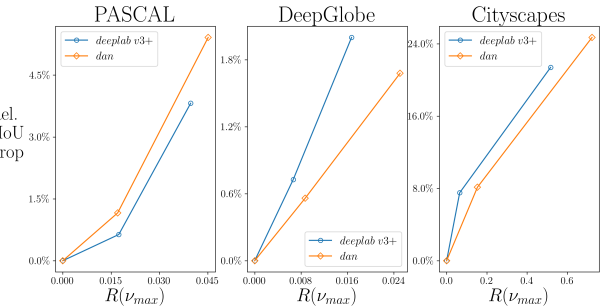


Figure 9: The correlation between relative mIoU-drop and the $R(\nu_{max})$ for the feature truncation. The results are evaluated based on PASCAL, DeepGlobe and Cityscapes datasets.

Feature size	PASCAL		DeepGlobe		Cityscapes	
	mIoU	relative mIoU-drop	mIoU	relative mIoU-drop	mIoU	relative mIoU-drop
Baseline						
129	78.5%	0.0%	55.0%	0.0%	67.8%	0.0%
65	78.1%	0.5%	54.6%	0.7%	62.7%	7.4%
33	75.6%	3.6%	53.9%	2.0%	53.3%	21.3%
20% Pruning rate for encoder						
129	76.6%	0.0%	53.7%	0.0%	67.2%	0.0%
65	76.0%	0.8%	53.4%	0.7%	62.4%	7.1%
33	73.2%	4.4%	52.7%	2.0%	53.4%	20.5%
40% Pruning rate for encoder						
129	74.4%	0.0%	53.0%	0.0%	66.1%	0.0%
65	73.9%	0.7%	52.7%	0.6%	61.5%	7.0%
33	72.1%	3.1%	52.0%	1.9%	52.8%	20.1%
60% Pruning rate for encoder						
129	65.1%	0.0%	50.1%	0.0%	58.6%	0.0%
65	64.7%	0.6%	49.9%	0.4%	54.8%	6.5%
33	63.3%	2.8%	49.4%	1.4%	47.4%	19.2%
(a) DeepLab v3+						
Feature size	PASCAL		DeepGlobe		Cityscapes	
	mIoU	relative mIoU-drop	mIoU	relative mIoU-drop	mIoU	relative mIoU-drop
Baseline						
129	77.6%	0.0%	53.6%	0.0%	66.4%	0.0%
65	76.7%	1.1%	53.3%	0.5%	61.0%	8.1%
33	73.4%	5.4%	52.7%	1.7%	50.0%	24.8%
20% Pruning rate for encoder						
129	76.8%	0.0%	53.6%	0.0%	65.8%	0.0%
65	75.9%	1.1%	53.2%	0.8%	60.3%	8.3%
33	72.8%	5.2%	52.4%	2.2%	49.0%	25.5%
40% Pruning rate for encoder						
129	74.6%	0.0%	52.3%	0.0%	65.1%	0.0%
65	73.8%	1.0%	51.9%	0.8%	59.8%	8.1%
33	71.3%	4.4%	50.7%	2.9%	48.9%	24.9%
60% Pruning rate for encoder						
129	65.6%	0.0%	49.5%	0.0%	57.0%	0.0%
65	65.1%	0.7%	49.4%	0.3%	52.4%	8.1%
33	63.0%	3.9%	48.9%	1.4%	42.8%	24.9%

(b) DAN						

Table 4: Results for feature truncation and network pruning on DeepLab v3+ and DAN. We summarize the results of using 4 setups of network pruning: "Baseline" denote the experiment without SFP while "X pruning rate for encoder" denotes that with SFP where X = (20%, 40%, and 60%) are the pruning rates. For each setup of network pruning, we further evaluate the results with 3 feature sizes for feature truncation, *i.e.* (129,65,33).

B Acknowledgement

Authors acknowledge the support of the Ministry of Science and Technology of Taiwan (MOST110-2115-M-A49-003-MY2).

References

[Ahn and Kwak 2018] Ahn, J., and Kwak, S. 2018. Learning pixel-level semantic affinity with image-level supervision for weakly supervised semantic segmentation. In *IEEE Conference on Computer Vision and Pattern Recognition (CVPR)*, 4981–4990.

[Badrinarayanan, Kendall, and Cipolla 2017] Badrinarayanan, V.; Kendall, A.; and Cipolla, R. 2017. Segnet: A deep convolutional encoder-decoder architecture for image segmentation. *IEEE Transactions on Pattern Analysis and Machine Intelligence (TPAMI)*.

[Blalock et al. 2020] Blalock, D.; Gonzalez Ortiz, J. J.; Frankle, J.; and Guttig, J. 2020. What is the state of neural network pruning? *Proceedings of machine learning and systems* 2:129–146.

[Caesar, Uijlings, and Ferrari 2018] Caesar, H.; Uijlings, J.; and Ferrari, V. 2018. Coco-stuff: Thing and stuff classes in context. In *IEEE Conference on Computer Vision and Pattern Recognition (CVPR)*.

[Chen et al. 2014] Chen, L.-C.; Papandreou, G.; Kokkinos, I.; Murphy, K.; and Yuille, A. L. 2014. Semantic image segmentation with deep convolutional nets and fully connected crfs. *ArXiv:1412.7062*.

[Chen et al. 2017] Chen, L.-C.; Papandreou, G.; Schroff, F.; and Adam, H. 2017. Rethinking atrous convolution for semantic image segmentation. *ArXiv:1706.05587*.

[Chen et al. 2018] Chen, L.-C.; Zhu, Y.; Papandreou, G.; Schroff, F.; and Adam, H. 2018. Encoder-decoder with atrous separable convolution for semantic image segmentation. In *European Conference on Computer Vision (ECCV)*.

[Cheng et al. 2021] Cheng, B.; Girshick, R.; Dollár, P.; Berg, A. C.; and Kirillov, A. 2021. Boundary iou: Improving object-centric image segmentation evaluation. In *Proceedings of the IEEE/CVF Conference on Computer Vision and Pattern Recognition*, 15334–15342.

[Cordts et al. 2016] Cordts, M.; Omran, M.; Ramos, S.; Rehfeld, T.; Enzweiler, M.; Benenson, R.; Franke, U.; Roth, S.; and Schiele, B. 2016. The cityscapes dataset for semantic urban scene understanding. In *IEEE Conference on Computer Vision and Pattern Recognition (CVPR)*.

[Dai, He, and Sun 2015] Dai, J.; He, K.; and Sun, J. 2015. Boxsup: Exploiting bounding boxes to supervise convolutional networks for semantic segmentation. In *IEEE International Conference on Computer Vision (ICCV)*, 1635–1643.

[Demir et al. 2018] Demir, I.; Koperski, K.; Lindenbaum, D.; Pang, G.; Huang, J.; Basu, S.; Hughes, F.; Tuia, D.; and Raska, R. 2018. Deepglobe 2018: A challenge to parse the earth through satellite images. In *IEEE Conference on Computer Vision and Pattern Recognition Workshops (CVPR Workshops)*.

[Everingham et al. 2015] Everingham, M.; Eslami, S. A.; Van Gool, L.; Williams, C. K.; Winn, J.; and Zisserman, A. 2015. The pascal visual object classes challenge: A retrospective. *International Journal of Computer Vision (IJCV)*.

[Guo et al. 2021] Guo, Z.; Liao, W.; Xiao, Y.; Veelaert, P.; and Philips, W. 2021. Weak segmentation supervised deep neural networks for pedestrian detection. *Pattern Recognition* 108063.

[Han et al. 2015] Han, S.; Pool, J.; Tran, J.; and Dally, W. 2015. Learning both weights and connections for efficient neural network. *Advances in neural information processing systems* 28.

[Hariharan et al. 2011] Hariharan, B.; Arbelaez, P.; Bourdev, L.; Maji, S.; and Malik, J. 2011. Semantic contours from inverse detectors. In *IEEE International Conference on Computer Vision (ICCV)*.

[He et al. 2016] He, K.; Zhang, X.; Ren, S.; and Sun, J. 2016. Deep residual learning for image recognition. In *IEEE Conference on Computer Vision and Pattern Recognition (CVPR)*.

[He et al. 2019] He, Y.; Dong, X.; Kang, G.; Fu, Y.; Yan, C.; and Yang, Y. 2019. Asymptotic soft filter pruning for deep convolutional neural networks. *IEEE Transactions on Cybernetics*.

[Jacot, Gabriel, and Hongler 2018] Jacot, A.; Gabriel, F.; and Hongler, C. 2018. Neural tangent kernel: Convergence and generalization in neural networks. *Advances in neural information processing systems* 31.

[Jing, Chen, and Tian 2019] Jing, L.; Chen, Y.; and Tian, Y. 2019. Coarse-to-fine semantic segmentation from image-level labels. *IEEE Transactions on Image Processing (TIP)* 29:225–236.

[Karnin 1990] Karnin, E. D. 1990. A simple procedure for pruning back-propagation trained neural networks. *IEEE transactions on neural networks* 1(2):239–242.

[Khoreva et al. 2017] Khoreva, A.; Benenson, R.; Hosang, J.; Hein, M.; and Schiele, B. 2017. Simple does it: Weakly supervised instance and semantic segmentation. In *IEEE Conference on Computer Vision and Pattern Recognition (CVPR)*.

[Kirillov et al. 2019] Kirillov, A.; Wu, Y.; He, K.; and Girshick, R. 2019. Pointrend: Image segmentation as rendering. *ArXiv:1912.08193*.

[Krähenbühl and Koltun 2011] Krähenbühl, P., and Koltun, V. 2011. Efficient inference in fully connected crfs with gaussian edge potentials. In *Advances in Neural Information Processing Systems (NIPS)*.

[Krizhevsky, Hinton, and others 2009] Krizhevsky, A.; Hinton, G.; et al. 2009. Learning multiple layers of features from tiny images.

[Kuo et al. 2018] Kuo, T.-S.; Tseng, K.-S.; Yan, J.-W.; Liu, Y.-C.; and Wang, Y.-C. F. 2018. Deep aggregation net for land cover classification. In *IEEE Conference on Computer Vision and Pattern Recognition Workshops (CVPR Workshops)*.

[Liu et al. 2019] Liu, Z.; Sun, M.; Zhou, T.; Huang, G.; and Darrell, T. 2019. Rethinking the value of network pruning. In *International Conference on Learning Representations (ICLR)*.

[Long, Shelhamer, and Darrell 2015] Long, J.; Shelhamer, E.; and Darrell, T. 2015. Fully convolutional networks for semantic segmentation. In *IEEE Conference on Computer Vision and Pattern Recognition (CVPR)*.

[Lu et al. 2021] Lu, W.; Gong, D.; Fu, K.; Sun, X.; Diao, W.; and Liu, L. 2021. Boundarymix: Generating pseudo-training images for improving segmentation with scribble annotations. *Pattern Recognition* 117:107924.

[Luo et al. 2019] Luo, T.; Ma, Z.; Xu, Z.-Q. J.; and Zhang, Y. 2019. Theory of the frequency principle for general deep neural networks. *arXiv preprint arXiv:1906.09235*.

[Luo, Wu, and Lin 2017] Luo, J.-H.; Wu, J.; and Lin, W. 2017. Thinet: A filter level pruning method for deep neural network compression. In *IEEE International Conference on Computer Vision (ICCV)*, 5058–5066.

[Molchanov et al. 2019] Molchanov, P.; Mallya, A.; Tyree, S.; Frosio, I.; and Kautz, J. 2019. Importance estimation for neural network pruning. In *IEEE Conference on Computer Vision and Pattern Recognition (CVPR)*.

[Mottaghi et al. 2014] Mottaghi, R.; Chen, X.; Liu, X.; Cho, N.-G.; Lee, S.-W.; Fidler, S.; Urtasun, R.; and Yuille, A. 2014. The role of context for object detection and semantic segmentation in the wild. In *IEEE Conference on Computer Vision and Pattern Recognition (CVPR)*.

[Nivaggioli and Randrianarivo 2019] Nivaggioli, A., and Randrianarivo, H. 2019. Weakly supervised semantic segmentation of satellite images. In *Joint Urban Remote Sensing Event (JURSE)*.

[Noh, Hong, and Han 2015] Noh, H.; Hong, S.; and Han, B. 2015. Learning deconvolution network for semantic segmentation. In *2015 IEEE International Conference on Computer Vision (ICCV)*, 1520–1528.

[Papandreou et al. 2015] Papandreou, G.; Chen, L.-C.; Murphy, K. P.; and Yuille, A. L. 2015. Weakly-and semi-supervised learning of a deep convolutional network for semantic image segmentation. In *IEEE Conference on Computer Vision and Pattern Recognition (CVPR)*.

[Rahaman et al. 2018] Rahaman, N.; Baratin, A.; Arpit, D.; Draxler, F.; Lin, M.; Hamprecht, F. A.; Bengio, Y.; and Courville, A. 2018. On the spectral bias of neural networks. *arXiv preprint arXiv:1806.08734*.

[Ronen et al. 2019] Ronen, B.; Jacobs, D.; Kasten, Y.; and Kritchman, S. 2019. The convergence rate of neural networks for learned functions of different frequencies. In *Advances in Neural Information Processing Systems*, 4763–4772.

[Ronneberger, Fischer, and Brox 2015] Ronneberger, O.; Fischer, P.; and Brox, T. 2015. U-net: Convolutional networks for biomedical image segmentation. In *International Conference on Medical image computing and computer-assisted intervention (MICCAI)*.

[Russakovsky et al. 2015] Russakovsky, O.; Deng, J.; Su, H.; Krause, J.; Satheesh, S.; Ma, S.; Huang, Z.; Karpathy, A.; Khosla, A.; Bernstein, M.; et al. 2015. Imagenet large scale visual recognition challenge. *International Journal of Computer Vision (IJCV)* 115(3):211–252.

[Shimoda and Yanai 2019] Shimoda, W., and Yanai, K. 2019. Self-supervised difference detection for refinement crf and seed interpolation. In *IEEE Conference on Computer Vision and Pattern Recognition Workshops (CVPR Workshops)*.

[Sun et al. 2019] Sun, T.; Tai, L.; Gao, Z.; Liu, M.; and Yeung, D.-Y. 2019. Fully using classifiers for weakly supervised semantic segmentation with modified cues. *arXiv preprint arXiv:1904.01749*.

[Xu et al. 2019] Xu, Z.-Q. J.; Zhang, Y.; Luo, T.; Xiao, Y.; and Ma, Z. 2019. Frequency principle: Fourier analysis sheds light on deep neural networks. *arXiv preprint arXiv:1901.06523*.

[Yang and Salman 2019] Yang, G., and Salman, H. 2019. A fine-grained spectral perspective on neural networks. *arXiv preprint arXiv:1907.10599*.

[Yang et al. 2018] Yang, M.; Yu, K.; Zhang, C.; Li, Z.; and Yang, K. 2018. Denseaspp for semantic segmentation in street scenes. In *2018 IEEE/CVF Conference on Computer Vision and Pattern Recognition*, 3684–3692.

[Yu and Koltun 2015] Yu, F., and Koltun, V. 2015. Multi-scale context aggregation by dilated convolutions. *arXiv preprint arXiv:1511.07122*.

[Zhao et al. 2017] Zhao, H.; Shi, J.; Qi, X.; Wang, X.; and Jia, J. 2017. Pyramid scene parsing network. In *IEEE Conference on Computer Vision and Pattern Recognition (CVPR)*.

[Zhao et al. 2019] Zhao, C.; Ni, B.; Zhang, J.; Zhao, Q.; Zhang, W.; and Tian, Q. 2019. Variational convolutional neural network pruning. In *IEEE Conference on Computer Vision and Pattern Recognition (CVPR)*, 2780–2789.

[Zhou et al. 2017] Zhou, B.; Zhao, H.; Puig, X.; Fidler, S.; Barriuso, A.; and Torralba, A. 2017. Scene parsing through ade20k dataset. In *IEEE Conference on Computer Vision and Pattern Recognition (CVPR)*.

[Zhou et al. 2019] Zhou, H.; Song, K.; Zhang, X.; Gui, W.; and Qian, Q. 2019. Wails: Watershed algorithm with image-level supervision for weakly supervised semantic segmentation. *IEEE Access* 7:42745–42756.